Biochimie 228 (2025) 114–126

Contents lists available at ScienceDirect

Biochimie

journal homepage: www.elsevier.com/locate/biochi

Mutations in the N-domain of aryl hydrocarbon receptor interacting protein affect interactions with heat shock protein 90β and phosphodiesterase 4A5

Marita Vella [a], Iain W. Manfield [b], Brandon C. Seychell [a], Chi H. Trinh [b], Robert Rambo [c], G. Nasir Khan [b], Josanne Vassallo [d], Thérèse Hunter [a], Gary J. Hunter [a, *]

[a] Department of Physiology & Biochemistry, Faculty of Medicine & Surgery, University of Malta, Msida, MSD2080, Malta
[b] Astbury Centre for Structural Molecular Biology, School of Molecular and Cellular Biology, Faculty of Biological Sciences, University of Leeds, Leeds, LS2 9JT, UK
[c] Soft Condensed Matter Group, Diamond Light Source Ltd, Diamond House, Harwell Science and Innovation Campus, Didcot, Oxfordshire, OX11 0DE, UK
[d] Department of Medicine, Faculty of Medicine & Surgery, University of Malta, Msida, MSD2080, Malta

ARTICLE INFO

Article history:
Received 4 July 2024
Received in revised form
3 September 2024
Accepted 13 September 2024
Available online 18 September 2024

Handling editor: Xavier Coumoul

Keywords:
Aryl hydrocarbon receptor interacting protein
hsp90
Phosphodiesterase
N-domain mutations
Protein:Protein Interactions

ABSTRACT

The aryl hydrocarbon receptor interacting protein (AIP) is a cytoplasmic molecular co-chaperone and tumour suppressor that assists in protein stability and complex formation involving the aryl hydrocarbon receptor. Germline mutations in the AIP gene predispose to pituitary tumourigenesis with patients exhibiting an aggressive clinical phenotype. Full length AIP proteins harbouring N-domain mutations (R9Q, R16H, V49 M and K103R) were purified from *E.coli* utilizing a methodology that maintained structural integrity and monomeric stability. Mutations did not significantly affect the thermal stability of the protein and caused no overall disruptive effect in the protein structure. The mutations studied lowered the binding affinity of AIP towards two of its binding partners; heat shock protein 90β and phosphodiesterase 4A5 (PDE4A5). The inhibition of phosphodiesterase activity by AIP was also greatly reduced by all mutants. While previously published data has mainly concentrated on the tetratricopeptide repeats of the C-domain of AIP, we present clear evidence that AIP N-domain mutations play a significant role in two protein:protein interactions with partner proteins. The complex interactome of AIP suggests that any observable change in one or more of its binding partners cannot be disregarded as it may have repercussions on other biochemical pathways.

1. Introduction

The aryl hydrocarbon receptor interacting protein (AIP, XAP2, ARA9) is a ubiquitously expressed cytoplasmic co-chaperone [1–3] and tumour suppressor [4,5]. It is a 37 kDa (330 amino acid) protein composed of an N-terminal peptidyl-prolyl *cis*-trans isomerase (PPIase)-like domain with no PPIase activity and C-terminal domain comprised of three tetratricopeptide repeat (TPR) motifs and a C-terminal 7 helix [6–8]. AIP is best known for its interaction with the aryl hydrocarbon receptor (AhR) that responds to exogenous toxins such as dioxins and endogenous ligands [9,10]. AIP plays a role in the regulation of cellular cAMP levels, oestrogen receptor signaling and cell survival, through its interaction with phosphodiesterase [5,11,12], Gα-proteins [13], the oestrogen receptor [14], the RET protooncogene [15] and survivin [16].

Mutations in AIP are associated with a predisposition to pituitary adenomas [4,17], with AIP-mutation positive patients displaying a more aggressive clinical phenotype and a young onset of the disease [18–20]. The identification of an AIP-variant and loss of heterozygosity in a follicular thyroid carcinoma specimen suggests that AIP might also have a potential role as an initiating event to thyroid carcinomas [21]. More recently, AIP has been found to be over-expressed in highly metastatic human colorectal cancer (CRC)

Abbreviations: AIP, aryl hydrocarbon receptor interacting protein; AhR, aryl hydrocarbon receptor; BA, benzyl alcohol; CD, circular dichroism; AIP, hexahistidine tagged AIP; SUMO-AIP, hexahistidine and SUMO tagged AIP; Hsp90CTD, Hsp90β$^{(530\text{-}724)}$; pET-AIP, pETite-NHis-SUMO-AIP; pET28-hsp90, pET28-hsp90β$^{(530\text{-}724)}$; PDE4A5, phosphodiesterase 4A5; SUMO-PDE4A5, hexahistidine and SUMO tagged PDE4A5.

* Corresponding author.
E-mail address: gary.hunter@um.edu.mt (G.J. Hunter).

https://doi.org/10.1016/j.biochi.2024.09.005

cells with evidence showing that AIP regulates the tumorigenic and metastatic properties of CRCs by dysregulation of epithelial-to-mesenchymal markers, driving liver metastasis [22]. High AIP expression has been observed in gastric cancer [23] and pancreatic tumours [24]. AIP may thus act as either an oncogene or a tumour suppressor protein depending on the type of cancer [25,26]. Moreover, AIP has been found to play a role in innate and adaptive immunity through its interaction with the transcription factor interferon regulatory factor 7 (IRF7) [27] and CARMA1 [28] respectively, with recent studies suggesting other immune functions which are yet to be explored [25,27]. Over the past decade more than 50 *AIP* gene mutations have been identified, with most missense mutations affecting the two final TPR motifs of the C-domain or the C-terminal α-7 helix [8,29]. Consequently, clinical mutations in the C-domain of AIP have attracted attention due to the domain's assumed direct involvement in protein-protein interactions [30], whilst the N-domain was believed to be responsible for conferring protein stability. However, further studies have identified the N-domain to also play an important role in protein:protein interactions, particularly with Hsp90 [7] and the scaffolding protein CARMA1, the latter being dependent only on the N-domain of AIP for interaction [28]. Two N-domain mutations (R16H and V49 M) have been associated with an aberrant apoptosis pathway involving the RET kinase and PIT1 transcription factor [31].

Here we investigate the structure and physicochemical properties of the full-length AIP and four specific N-domains mutants of clinical relevance: R9Q, R16H, V49 M and K103R. Although these mutations have been previously reported [12,32], no study is currently available that compares *in vitro* protein stability and/or the binding affinities of AIP with those of its mutant counterparts. We demonstrate how these N-domain mutations affect the protein's ability to bind to Hsp90 C-terminal domain (Hsp90CTD) or PDE4A5, thereby highlighting the involvement of the N-domain in protein:protein interactions.

2. Material and methods

2.1. Expression plasmids for AIP, Hsp90CTD and PDE4A5

A pcDNA3 vector harbouring the cDNA for human AIP was kindly provided by Dr Robert Formosa (University of Malta), which served as PCR template to amplify the full-length AIP coding region using primers pET-AIP-F and pET-AIP-R (Supplementary Materials Table S1). The cDNA for PDE4A5 (homologous rat isoform) cloned as a fusion to maltose-binding protein was a kind gift from Professor Graeme Bolger (University of Alabama USA). This served as a template to amplify PDE4A5 using primers PDE-F and PDE-R (Supplementary Materials Table S1). The amplicons produced for AIP and PDE4A5 were each cloned by homologous recombination into the pETite™ N-His SUMO vector using the Expresso® T7 SUMO Cloning and Expression System (Lucigen) to express SUMO fusion proteins. AIP and PDE clones were designated pET-AIP and pET-PDE. The cDNA for full-length AIP was also cloned into *Stu*I-cleaved pTH-1 [33], via blunt-end cloning to generate an N-terminal hexahistidine-tagged AIP protein, using primers AIP-F and AIP-R to generate the insert DNA by PCR. This clone was designated pTH-AIP. The clone pET28-Hsp90 harbouring the cDNA for Hsp90CTD was kindly provided by Professor Thomas Ratajczak (Department of Endocrinology & Diabetes, Western Australia) and designated pET-hsp90.

2.2. Site-directed mutagenesis

Recombinant pET-AIP plasmid was used as DNA template for the mutagenesis reactions, performed using the QuikChange II XL Site-Directed Mutagenesis Kit (Agilent Technologies). Mutagenic primer pair sequences are similarly listed in Supplementary Materials Table S1 and were used to generate mutations AIP[R9Q], AIP[R16H], AIP[V49 M], AIP[K103R] which were confirmed by Sanger sequencing (Bioneer) using SUMO-F and SUMO-R as sequencing primers. Recombinant pTH-AIP was also used as a template to generate the hexahistidine tagged AIP mutants. Sequencing results are found in Supplementary Materials Fig. S1.

2.3. Protein expression and purification

E.coli BL21 (DE3) CodonPlus (Novagen) transformed with pET-AIP was grown at 37 °C in 2TY media supplemented with kanamycin (50 μg mL^{-1}) and harvested 4 h after induction with 0.1 mM isopropyl β-*d*-1-thiogalactopyranoside (IPTG).Cells were re-suspended in ice-cold buffer consisting of 20 mM Tris-Cl pH 7.5, 100 mM NaCl, 5 mM DTT, cOmplete protease inhibitor tablet (Roche®) and 10 mM phenylmethylsulfonyl fluoride and lysed by French press. DNA was degraded by DNase A (0.01 mg mL^{-1}) supplemented with 5 mM $MgCl_2$ followed by sonication on ice using a Soniprep II 150 (MSE). After the addition of glycerol (10 % v/v), the lysate was clarified by centrifugation at 15,000 *g* for 30 min at 4 °C and loaded on a cOmplete™ His-Tag Purification Column (Roche). SUMO-AIP protein was eluted with 25 mM imidazole. *E.coli* strain BL21 (DE3) Codon Plus cells harbouring pTH-AIP were grown under the same experimental conditions. AIP was purified using the same protocol as outlined for the SUMO tagged counterpart. The molecular weight of the purified AIP and AIP mutants was confirmed by mass spectrometry using an Electro-Spray Mass Spectrometer for which samples were prepared in 50 mM ammonium acetate pH 7.4 at a concentration of 20 μM. Pure AIP protein was stored at −80 °C in 20 mM Tris-Cl pH 7.5, 100 mM NaCl, 10 % (v/v) glycerol and 1 mM DTT.

E.coli strain BL21 (DE3) CodonPlus (Novagen) transformed with pET28a-Hsp90 were grown in 2TY culture flasks supplemented with kanamycin (50 μg mL^{-1}) at 37 °C, induced with 0.4 mM IPTG and harvested 3 h after induction. Cell lysis and protein purification was carried out as described for AIP. Pure protein was stored at −80 °C in 10 mM Tris-Cl pH 7.5, 100 mM NaCl, 5 mM DTT as storage buffer.

Expression of SUMO-PDE4A5 was performed in *E.coli* BL21 (DE3) Rosetta cells (Novagen) that were grown at 37 °C in 2TY media supplemented with kanamycin (50 μg mL^{-1}). Benzyl alcohol (10 mM) was added 20 min prior to induction with 0.1 mM IPTG. $ZnSO_4$ (40 μM) was added at the point of induction and cells were harvested after 3 h. The protein was purified using Ni-NTA affinity column. Pure PDE4A5 was stored at −80 °C in 20 mM Tris-Cl pH 8.0, 100 mM NaCl, 5 % (v/v) glycerol, 1 mM TCEP.

All proteins were further purified by size exclusion chromatography on Superdex 75 column prior to further analysis. For each protein, purity was assessed by densitometry of SDS-PAGE gels stained by Coomassie Brilliant Blue R-250.

2.4. Protein stability studies

Samples of SUMO-AIP at 1 mg mL^{-1} were prepared in 20 mM Tris-Cl pH 7.5, 100 mM NaCl, to which different additive concentrations was added. Following overnight incubation, soluble protein was separated from any protein aggregates by centrifugation at 16,000 *g* for 15 min. The possible formation of aggregates was checked by Native-PAGE (8 %) stained with Coomasie Brilliant Blue R-250. Further stability experiments were performed on an *Optim*®1000 instrument (Avacta Innovative Analysis UK). Aliquots of each sample (10 μL) were loaded onto the *Optim*®1000

compatible micro-cuvette arrays (MCAs). The machine was programmed to monitor the static light scattering (SLS) from a 266 nm and 473 nm laser source. The sample temperature was increased from 15 °C to 90 °C in 1 °C step intervals with a 30 s hold prior to each temperature change. The SLS signal was recorded at each temperature point. The change in fluorescence emission of tryptophan was measured through the barycentric mean fluorescence (λ_{BCM}). The generated data was analysed using the *Optim*®1000 Analysis Software version 2.0 (Avacta Analytical) (Supplementary Materials Fig. S2).

2.5. Circular dichroism spectroscopy

Far-UV CD spectra (180–260 nm) using a 1 mm path length and near-UV CD spectra (250–320 nm) using a 10 mm path length were collected using a Chirascan™ CD-Spectrometer (Applied Photophysics). The melting temperature of each sample was determined by a continuous temperature scan, from 5 °C to 90 °C with 5 °C increments and a 2 min hold prior to each temperature change. Protein samples were prepared at a concentration ranging between 0.1 and 0.2 mg mL^{-1} in 10 mM potassium phosphate (KP) pH 7.8. Melting temperatures were determined using CD data at a fixed wavelength of 222 nm. Normalised data was fitted using a non-linear regression with a least squares fitting method and a Boltzmann Sigmoidal equation. The confidence level was set at 95 %. All CD analyses were performed using GraphPad Prism Version 8.0.

2.6. Mass photometry

For mass photometry measurements samples of purified Hsp90CTD were diluted to nanomolar concentrations (ranging from 20 to 50 nM) using 1x PBS as the dilution buffer, prior to use. Data was acquired using the mass photometry facility (Acquire™, Refeyn) at EMBL Hamburg. Measurements were conducted according to standard protocol [34] and data analysed using Discover^{MP} software supplied with the machine.

2.7. Isothermal titration calorimetry

ITC experiments were performed at 25 °C in an ITC200 microcalorimeter (MicroCal) in 20 mM Tris-Cl pH7.5, 5 mM NaCl, 5 % (v/v) glycerol. Hsp90CTD (150 μM) was titrated into the reaction cell containing AIP (6 μM), dialysed against the same buffer (0.5 μl then 19 injections of 2 μl). The same injection was repeated for every AIP mutant. The heat of dilution of titrant into buffer was determined in a separate experiment and the corrected data was fitted using the one set of sites curve fitting model (MicoCal Origin) (Supplementary Materials Fig. S3). Furthermore, mass photometry demonstrated that Hsp90CTD dilution resulted in predominantly dimer formation (Supplementary Materials Fig. S4) so this was assumed for ITC data interpretation.

2.8. Surface plasmon resonance

SPR experiments were performed at 25 °C using a Biacore 2000 instrument (GE Healthcare Life Sciences). Protein immobilisation was performed using amine coupling chemistry on CM5 sensor chips. Hsp90CTD and SUMO-PDE4A5 (50 μg mL^{-1}) were injected for 5 min at a constant flow rate of 5 μL min^{-1} over the NHS/EDC-activated surface. Protein interaction analysis was performed at 25 °C in 1 x PBS pH 7.4 containing 0.1 % surface polysorbate 20. SUMO-AIP and mutants were sequentially injected for 3 min at a flow rate of 40 μL min^{-1}, followed by a 5 min dissociation phase. Pure SUMO protein was used as control. The concentration of each analyte was gradually increased from 20 nM to 20 μM. For both AIP-Hsp90CTD and AIP-PDE4A5 interactions, a series of injections was performed with increasing analyte concentration, starting with 20 nM as the first injection. Subsequent injections were performed at a concentration of 40 nM, 100 nM, 200 nM, 500 nM, 1 μM, 2.5 μM, 5 μM, 10 μM and 20 μM (Supplementary Materials Fig. S5 and Fig. S6). The overlaid curves were x- and y-transformed. This aligned each curve at the start of injection and adjusted them to the same baseline. Only the first minute of the dissociation phase (185–245 s) was used for curve fitting analyses. The remaining 4 min were carried out to ensure that the analyte was washed off the surface prior to the next analyte injection (chip-regeneration). Curve fitting and kinetic data analyses were evaluated with BIAevaluation software version 3.1.

2.9. PDE-Glo™ Phosphodiesterase Assay

AIP was added to PDE4A (Bio-Techne) in a final volume of 12.5 μL and incubated for 20 min at room temperature, prior to the addition of cAMP (2 μM). The rest of the procedure was carried out according to manufacturer's instructions, PDE-Glo™ Phosphodiesterase Assay (Promega). Data was graphically plotted using GraphPad Prism software Version 8.0. Statistical analyses were carried out using SPSS Statistics Version 20 (IBM). The distribution of the data was checked using the Shapiro-Wilk and Kolmogorov-Smirnov test. Parametric tests were used for normally distributed data. These included the independent *t*-test and one-way ANOVA, set at a confidence level of 95 %.

2.10. Size-exclusion chromatography small angle X-ray scattering (SEC-SAXS)

Samples of pure AIP[R9Q] and SUMO-AIP in 20 mM Tris-Cl pH 7.5, 100 mM NaCl, 1 mM DTT, 5 % (v/v) glycerol were initially analysed in batch using 30 μL samples flowing at 1 μL per second. For SEC-SAXS, 50 μL of the sample that showed the best scattering profile was loaded on a pre-calibrated Shodex KW403–4F gel filtration column (Agilent 1200 HPLC system), set at a flow rate of 0.08 mL min^{-1} and 1 s exposure time. SAXS data was analysed using ScÅtter Version 3.0, a JAVA-based application [35]. The quality of the data was assessed through the Kratky plot, Guinier Analysis and Porod plot. A homology model of AIP using PDB entries 2LKN (PPIase domain) and 4AIF (TPR domain) was made with the SWISS-MODEL [36] server. The homology model provides a sequence correct, atomistic model that was subsequently used in a constrained molecular dynamics (MD) simulation. The model consists of two domains, connected by a single, peptide linker with N- and C-terminal tails. MD simulations were performed with CNS [37,38]. Distance constraints derived from the SAXS-based paired-distance, P(r), distribution function were used to constrain the interdomain distance during several rounds of simulated annealing. Secondary structure prediction and constraints for the unknown regions of the protein sequence were determined using SPIDER2 [39,40]. The constraints were encoded as pseudo-NOE restraints with upper and lower bounds defined by the Shannon sampling theorem (π/q_{max}). Tails were not allowed to exceed SAXS-determined maximum dimension (d_{max}). Several rounds of simulated annealing were performed by heating to 50000 K and slow cooling to 0 K in 5000 steps. This allowed sampling of the interdomain distance and relative orientations. The theoretical scattering profiles of the generated models were computationally compared to the experimental one and the best model identified using FoXS [41]. All SAXS

data were collected at beamline B21 at Diamond Light Source, UK's national synchrotron science facility situated at the Harwell Centre for Research and Innovation, Oxford. Subsequent analysis on the SAXS generated model was done using PyMOL version 2.6.0 [42] and SWISS-PDB Viewer version 4.1 [43].

3. Results

3.1. Protein expression and purification

AIP proteins were expressed and affinity purified to homogeneity, reaching purity levels of 90–93 %. H_6-tagged proteins reached their maximal purity levels after one round of purification on the Ni-NTA column (Fig. 1A and B), whereas SUMO-tagged counterparts required two consecutive rounds to attain similar levels. Yields of protein from Ni-NTA columns were 25 mg L^{-1} (His-SUMO tag) and 40 mg L^{-1} (His tag). The purity and homogeneity of the purified proteins were assessed by SDS-PAGE and Native-PAGE respectively and confirmed by immunoblotting (Fig. 1C, D, E, F, Supplementary Materials Fig. S7). While the purification of AIP and AIP domains has previously been reported [6,8], our procedure consistently produced high yields of stable, pure AIP. The absence of additives adversely affects protein quality and results in significant protein aggregation. The choice and concentration of additives were optimised using an Optim®1000 instrument (Supplementary Materials Fig. S2). Hsp90CTD was affinity purified by two rounds of Ni-NTA purification, attaining a purity of ≥95 % and a final yield of 29 mg L^{-1} of bacterial culture. The protein's molecular weight as determined from size exclusion chromatography was 48–49 kDa, corresponding to that of a dimer and confirmed by mass photometry (Supplementary Materials Fig. S4). Physiologically Hsp90 dimerisation is mediated through the C-domain, residues 599–724 [44]. SUMO-PDE4A5 was successfully expressed in the presence of benzyl alcohol (BA) and $ZnSO_4$ as additives and affinity purified attaining a purity of 87 % and a final yield of 5.6 mg L^{-1} of culture. BA, when present in low concentrations, causes transient fluidization of the *E.coli* cell membrane and up-regulates the transcription of target heat shock genes [45], inducing endogenous chaperone expression that may improve the yield and solubility of proteins [45,46]. The results obtained indicate that SUMO-PDE4A5 solubility was improved after benzyl alcohol addition (Supplementary Materials Fig. S8).

3.2. Protein stability and binding by circular dichroism spectrophotometry

Each AIP mutant exhibited a CD spectrum similar to the wild-type protein with negative peaks at 222 nm and 208 nm and a positive ellipticity at 193 nm, typical of helical proteins (Fig. 2 A). Hsp90CTD and SUMO-PDE4A5 CD results were indicative of folded proteins (Fig. 2 B). N-terminal mutations decreased AIP's thermal stability with the thermal transition midpoint of each mutant differing between 1.3 °C (R9Q) and 5.1 °C (V49 M) (Fig. 3, Supplementary Materials Fig. S9). Far-UV CD spectra of the AIP-Hsp90CTD mixture (Fig. 4 A) showed no change in ellipticity compared to the theoretical sum of individual spectra, suggesting that protein binding had not altered the secondary structure of either protein. The AIP-PDE4A5 spectrum exhibited changes around 205–208 nm and an increase in ellipticity at 222 nm, compared to the theoretical sum of individual spectra, suggestive of protein-protein interactions that result in secondary structure changes (Fig. 4 B).

3.3. Protein-protein interaction analyses of AIP with Hsp90CTD or PDE4A5

The binding affinities of SUMO-AIP to Hsp90CTD and SUMO-AIP to PDE4A5 interactions were analysed using surface plasmon resonance (SPR). AIP produced a positive SPR binding response indicative of binding to Hsp90CTD (>20 RU), at 1 μM or greater. AIP mutant V49 M showed a significant SPR signal only at 20 μM and higher (Supplementary Materials Fig. S5 and Fig. S6). For the AIP-PDE4A5 interaction, AIP displayed the highest binding affinity while mutants exhibited a 3-fold (R16H), 4-fold (R9Q and K103R) and 5~6-fold (V49 M) decrease towards the immobilized SUMO-PDE4A5 partner (Fig. 5 B and Table 1). SUMO (expressed from an empty vector) was utilized as a control (Fig. 5A and B) and

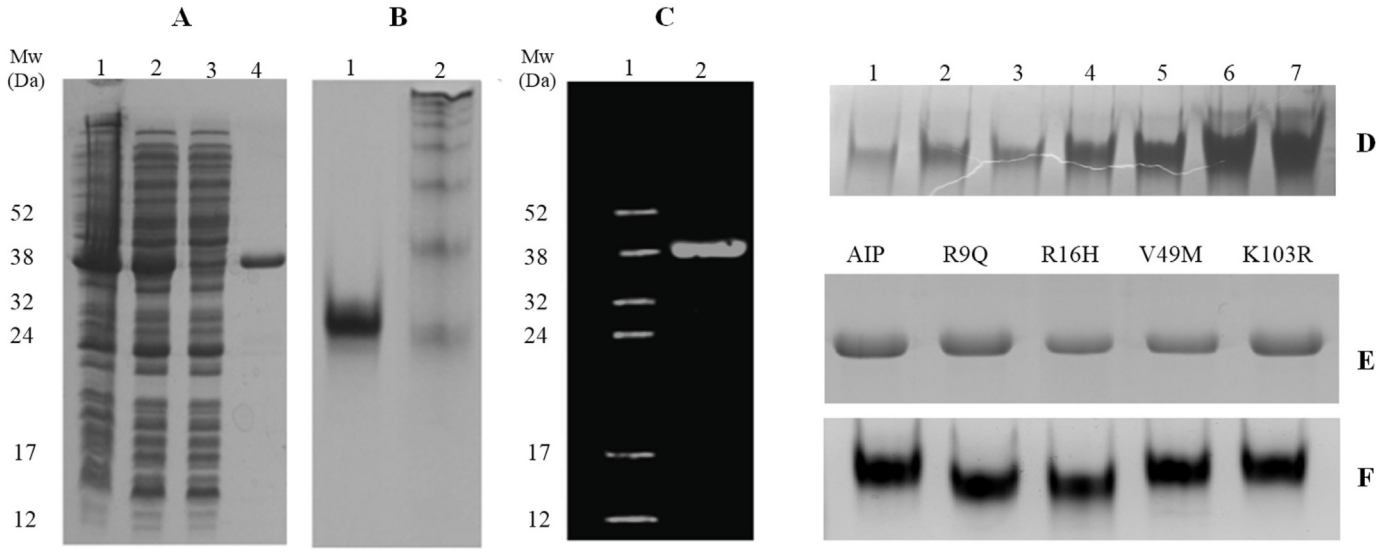

Fig. 1. Purification of AIP. A: 15 % SDS-PAGE analysis: Lane 1: Total cell lysate (20 μg), Lane 2: Clarified lysate (20 μg); Lane 3: Column flow-through (15 μg); Lane 4: Purified AIP (5 μg). B: 8 % Native-PAGE analysis: Lanes 1: AIP (5 μg) purified in the presence of 10 % glycerol and 5 mM DTT; Lane 2: AIP (5 μg) purified in the absence of glycerol and DTT. C: Immunoblotting using anti-his tag as 1° antibody: Lane 1: ECL Rainbow molecular weight markers (5 μL) (GE Healthcare), Lane 2: Pure AIP (5 μg). D: 8 % Native-PAGE analysis: SUMO-AIP at increasing concentrations ranging from 1 mg mL^{-1} (Lane 1) to 7 mg mL^{-1} (Lane 7) concentrated in the presence of glycerol and DTT. Pure AIP and AIP mutants (10 μg) on 15 % SDS-PAGE (E) and 8 % Native-PAGE (F) respectively.

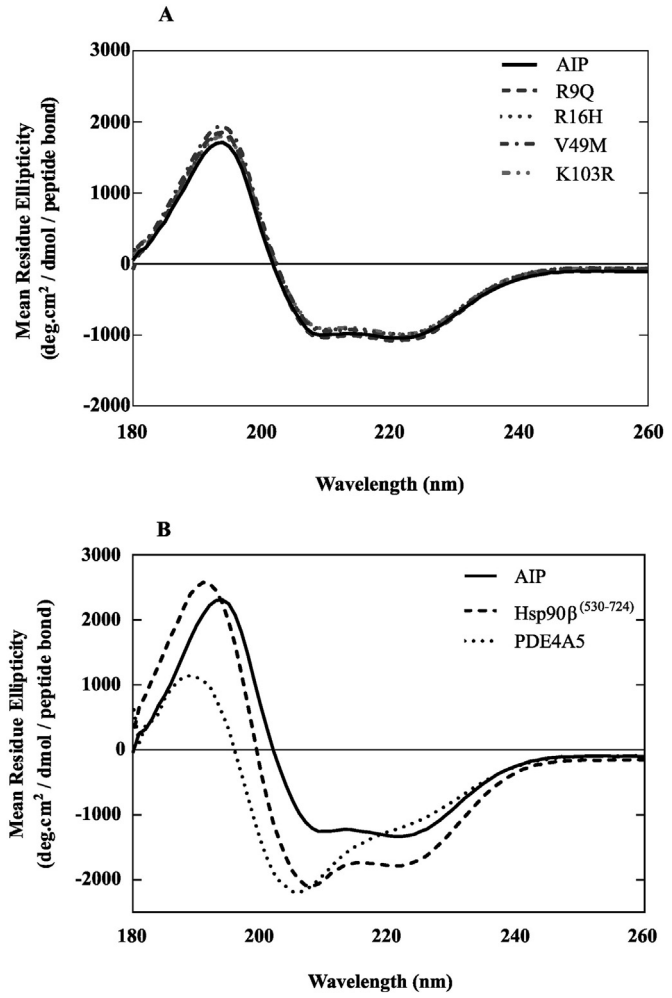

Fig. 2. Circular dichroism protein structure and stability analysis: A: Far-UV CD spectrum of AIP, Hsp90CTD and SUMO-PDE4A5. B: Far UV spectrum of AIP mutants. All proteins were prepared at an equal molar concentration of 2.5 μM.

confirmed that the SUMO-tag itself had no effect.

AIP demonstrated the strongest binding affinity to Hsp90CTD, with mutants exhibiting 2-fold (R9Q), 3~4-fold (R16H) and 3.5 ~ 5-fold (V49 M) weaker affinities (Fig. 5 A and Table 1). The AIP-Hsp90CTD interaction was further investigated through isothermal titration calorimetry (ITC) (Table 2 and Supplementary Materials Fig. S10 and Fig. S11). The strongest interaction was between Hsp90CTD and AIP. R9Q showed a 2-fold decrease in binding affinity, while R16H and V49 M displayed a 4-fold decrease and K103R had little effect. These data support those obtained through SPR (Table 1 and Supplementary Materials Fig. S5).

3.4. Phosphodiesterase activity assays

As AIP has an inhibitory effect on PDE4A5 [11,47], we therefore assessed the effect of AIP mutations on PDE4A5 phosphodiesterase activity. At equimolar concentrations, phosphodiesterase activity was inhibited 64 % by AIP in agreement with Bolger et al. (2003). R9Q inhibited phosphodiesterase activity by 34 %, R16H by 26 % and both V49 M and K103R by 18 %, with the enzyme retaining more than 80 % of its activity (Fig. 6A and B).

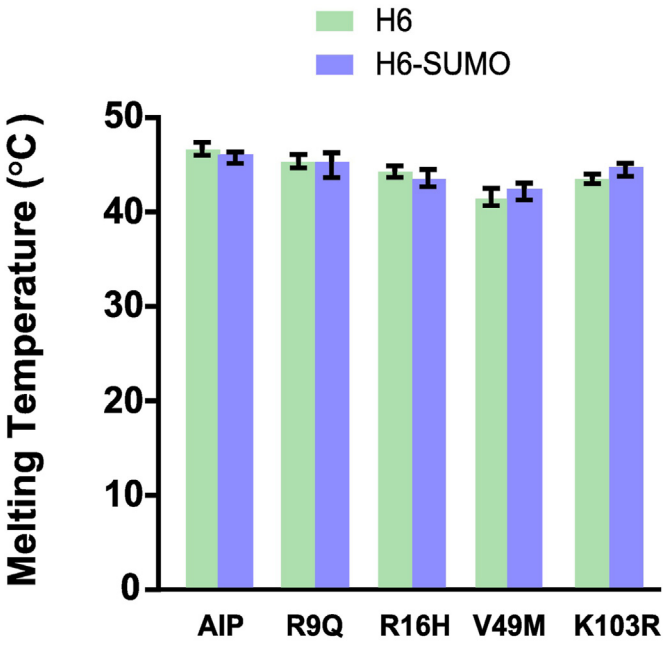

Fig. 3. Melting temperature determination of AIP and mutant derivatives. Values are derived from CD analysis (Supplementary Materials Fig. S9.).

3.5. Structural analyses of SAXS AIP model

Our structural model of AIP derived from small angle X-ray scattering (SAXS) shows that the two domains of AIP as previously determined by Linnert [6] and Morgan [8], have a preferred orientation where the loop region (G111-H135) of the PPIase domain is positioned towards the TPR domains (Figs. 7 and 8). In solution, our best fitting SAXS models suggest a linear arrangement of the two domains and suggests a system where the two domains are moving relative to one another. The predicted structure obtained through Alphafold3 [48] only agrees with this model if the C domain is reorientated into a more open, stretched form. This is quite possible due to the flexibility of the hinge region between domains and their observed mobility (Supplementary Materials Fig. S12).

In agreement with NMR data [6], the unstructured loop region (G111-H135) that is part of the βD-βE extension showed conformational variability. In addition, SAXS revealed that the relative position of this loop has a significant effect on the the computed structure and although it can take different conformations, only two models fit the SAXS scattering profile revealing the most stable forms that occur in solution and therefore those of physiological relevance (Fig. 8 and Supplementary Materials Figs. S13 and S14).

3.6. Effect of the mutations on the structure of AIP

The R9Q mutation resulted in the loss of surface positive charge and the introduction of a moderate electrostatic hydrogen bond (3.2 Å) between OE1 of Gln9 and main chain N of Lys15. This hydrogen bond connects the Gln9 residue in the α0 helix with the first β-strand (βA) of the half β-barrel, possibly limiting the mobility of the α0 region (Fig. 9). The R16H mutation also resulted in the partial loss of positive charge. Similarly, the introduction of histidine resulted in the formation of a moderate, mostly electrostatic interaction (2.9 Å) between ND1 of His16 and O of Val17. Both His16 and Val17 are part of the βA strand (Fig. 9). In the case of V49 M, the

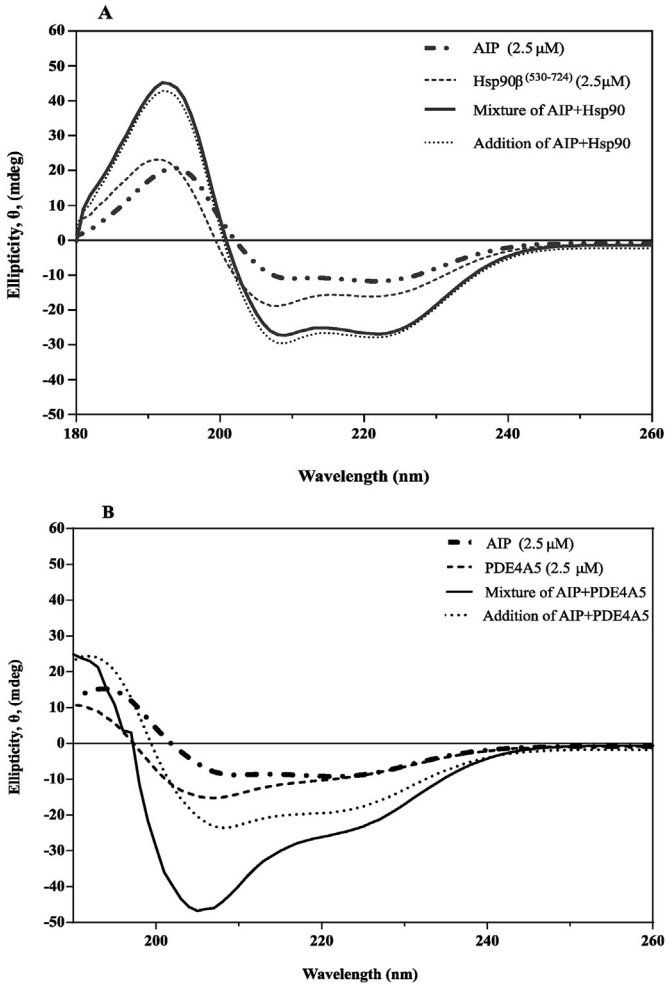

Fig. 4. Circular dichroism of protein: protein interactions. A: Far-UV CD spectra of AIP, Hsp90CTD. Solutions of AIP (5 μM) and Hsp90CTD (5 μM) were mixed in equal volumes and incubated for 1 h at 20 °C. B: Far-UV CD spectra of AIP, PDE4A5 and equimolar mixtures of the two purified proteins. Solutions of AIP (5 μM) and PDE4A5 (5 μM) were mixed in equal volumes and incubated for 1 h at 20 °C. In each mixture, the final molar concentration of each protein was diluted two fold by the presence of the second protein. The CD spectrum of each mixture (experimental CD, solid line) was compared to the spectrum of the sum of the individual proteins (expected CD, dotted line).

methionine side chain was in close enough proximity to form an interaction (2.6 Å) between SD of Met49 and OD1 of Asp52, both residues form part of the βC strand (Fig. 9). For K103R, the overall surface charge was minimally affected. Polar contact analyses demonstrated that the wild type protein has a moderate hydrogen bond of 3.4 Å between NZ of Lys103 and O of Pro99 (Fig. 9). Both Lys103 and Pro99 are found on the αIII helix that forms the first structural element of the βD-βE extension. While, this interaction is lost in the Arg103 mutant, a different interaction is formed that involves NH2 of Arg103 and OD1/OD2 of Asp139. Interesting, Asp139 is located on the αIV helical region that marks the end of the βD-βE extension. In the wild type protein, none of the amino acids in the αIII region form hydrogen bonds and/or salt bridges with the residues on the αIV helix. The absence of such interactions might partially account for the flexibility observed in the loop region that is found in between these two helical structures and therefore suggests that the interaction that is introduced in the Arg103 mutant might limit this mobility.

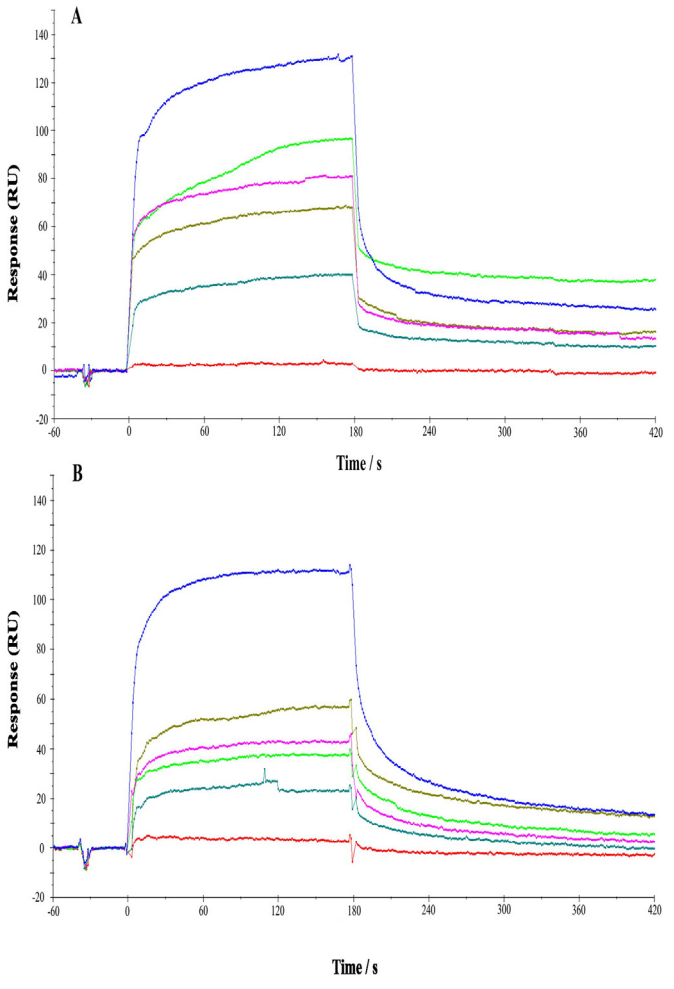

Fig. 5. SPR Sensorgram showing the binding of A: SUMO-AIP and mutants to Hsp90CTD; B: SUMO-AIP and mutants to SUMO-PDE4A5. SUMO-AIP/mutants at 20 μM were sequentially injected for 3 min over protein immobilized on CM5 sensor surfaces, followed by buffer flow to allow SUMO-AIP dissociation. A high-salt buffer injection was used to regenerate surfaces after each injection.

Table 1
Binding constants and statistical parameters for wild type AIP and mutants as obtained through SPR using the Langmuir 1:1 curve fitting model.

Ligand	Hsp90CTD		SUMO-PDE4A5	
Analyte	K_D (μM)	Chi^2	K_D (μM)	Chi^2
AIP	1.23	0.93	2.64	0.90
R9Q	3.29	1.13	10.5	0.59
R16H	3.97	0.84	8.04	0.88
V49 M	5.72	0.61	14.5	1.46
K103R	1.61	0.87	10.1	1.26

Table 2
Dissociation constants for the interaction between wild type AIP and mutants with Hsp90CTD as obtained through ITC.

Protein	n	K_D (μM)	ΔH (kcal.mol^{-1})	ΔS (cal mol^{-1} deg^{-1})
AIP	0.74 ± 0.16	2.19	−11.5 ± 3.2	−12.7
R9Q	0.70 ± 0.15	5.40	−8.7 ± 2.6	−5.13
R16H	0.53 ± 0.29	7.80	−23.7 ± 13.1	−16.1
V49 M	0.60 ± 0.40	10.70	−10.3 ± 9.3	−11.7
K103R	0.69 ± 0.07	2.88	−13.0 ± 2.0	−18.4

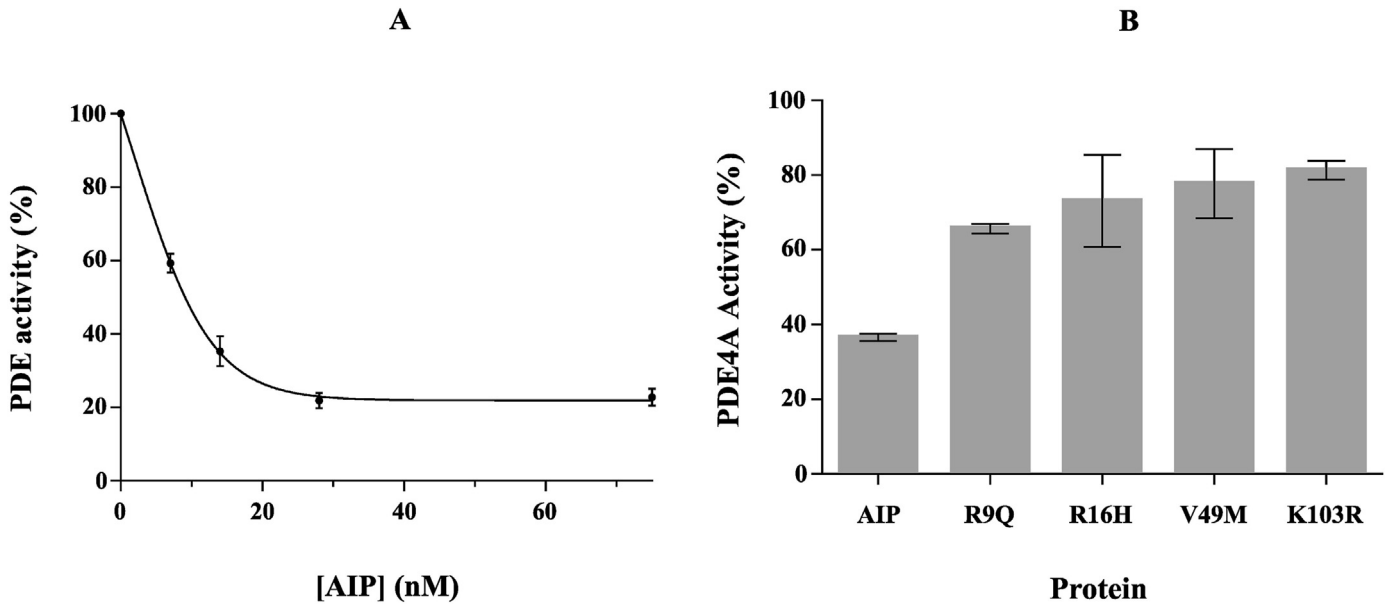

Fig. 6. Phosphodieasterase Activity Assay. A: Concentration-dependent PDE4A inhibition assay. Data was analysed using a non-linear regression, one-site specific binding with Hill slope equation. Each point represents the average of three replicates each (n = 3). B: Effect of AIP and AIP mutants on PDE4A inhibition assay. Each bar represents the mean of three experiments carried out on separate days with different batches of the same protein type (4 ng of protein used in each experiment). Samples were prepared in triplicates for reliability (n = 3). The AIP and AIP-mutants used in this experiment were hexahistidine tagged. In each Figure, error bars represent standard deviation (SD) and the reported differences were all statistically significant ($P < 0.05$).

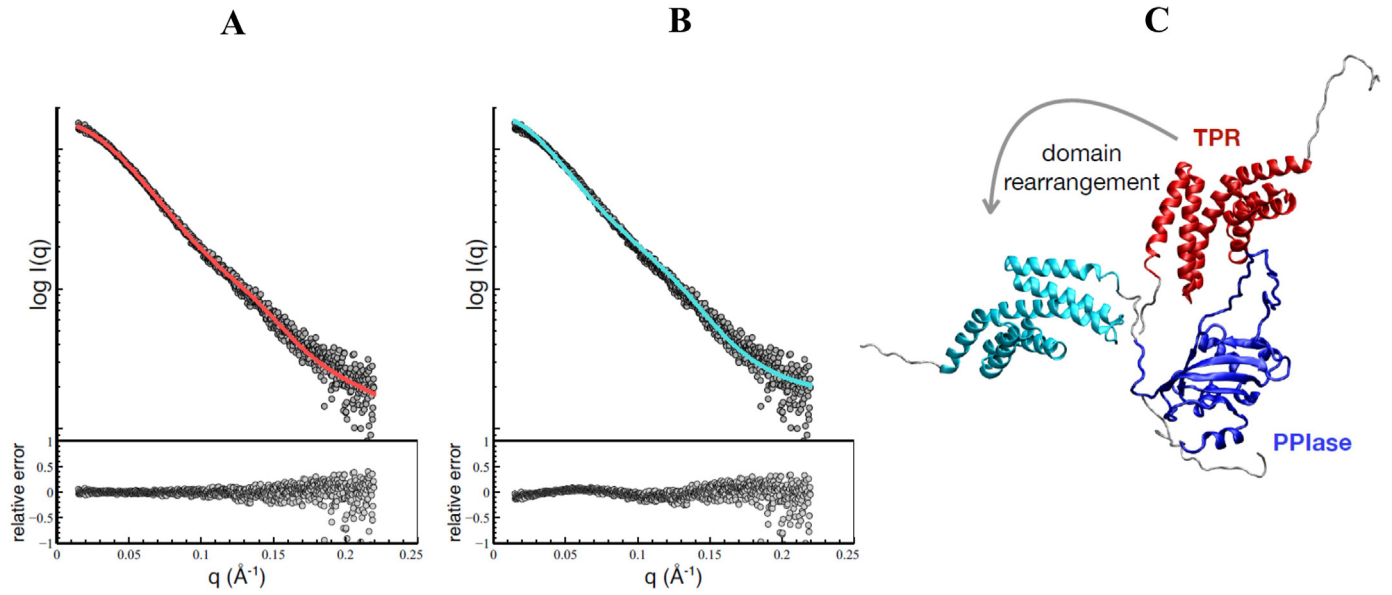

Fig. 7. SAXS analysis of AIP at 4.5 mg mL^{-1}. A: Fit of the best-fitting, refined atomistic model with a chi^2 of 1.72 (red). B: Fit of atomistic model with TPR domain in alternative orientation produces a chi^2 of 4.59 (cyan). Lower panels are residuals of each respective fit. C: Atomistic models from A and B. Best fitting model consist of blue and red domains oriented as shown. The alternative orientation of TPR (cyan) relative to PPIase is also shown. Fits were performed with FoXS.

4. Discussion

Our initial purification of AIP as a SUMO-AIP fusion protein resulted in good solubility and stability as expected [49]. However, removal of the SUMO tag and subsequent purification of native AIP resulted in such low solubility it was impractical to work with after storage. We therefore expressed AIP and mutants with a simple hexahistidine tag, enabling purification in a single, rapid procedure. This increased the yield of pure AIP by almost two-fold and allowed us to use the protein immediately after purification. CD showed little difference in thermal stability between AIP and SUMO-AIP (Fig. 3). AIP and mutants were purified using the same procedures, attaining purity levels of 88–93 %. The yield obtained from the purification of R16H and V49 M was always lower, suggesting that these two mutations may in some way destabilize the protein or reduce expression efficiency within the cell. The V49 M mutant has previously been reported to have a short half-life in HEK293 cells due to enhanced proteasomal degradation [50] but data for *E.coli* stability is not available. Similarly, cycloheximide chase experiments in GH3 cells transfected with wild-type AIP and N-domain

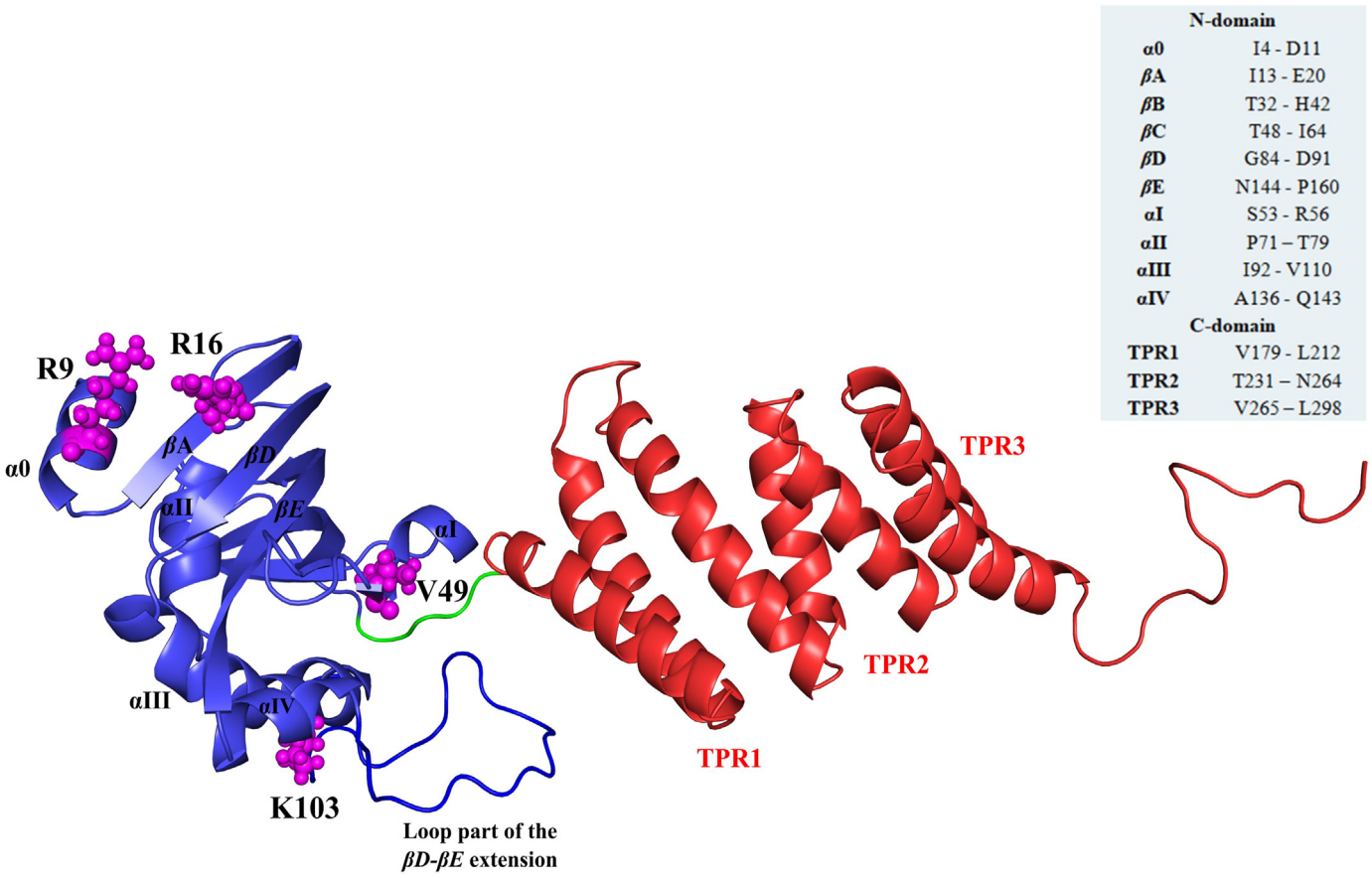

Fig. 8. Cartoon representation of the best fitting SAXS model of AIP. The N-domain (PDB 2LKN) and C-domain (PDB 4AIF) of AIP are shown in blue and red respectively, connected by a short linker (green). The flexible loop in the N-domain of AIP is shown in orange. The site of each N-domain mutation is indicated. The panel on the right indicates the respective location of each structural motif. This figure was generated using PyMOL version 2.6.0 [42].

mutants have demonstrated that the mutants R9Q, R16H and V49 M have a significantly higher rate of degradation, 28 h post-treatment, with reported half-lives of 18.5, 18.0 and 16.0 h respectively [32].

AIP mutants showed CD spectra which is highly similar to that of the wild type protein, indicating that all proteins had an ordered structure and that the N-terminal mutations investigated do not cause disruptive effect on the overall structure of AIP. While cell biology studies suggest that N-domain mutations destabilize AIP [32,50], our results demonstrate that this is not due to protein chemistry but implicates biological effectors as the cause. However, protein over-expression causes aggregation of proteins including AIP and mutants. We successfully reduced or prevented this by testing a series of additives at various concentrations (results not shown), and the addition of NaCl, DTT and glycerol was determined to be sufficient.

The interaction between AIP and Hsp90CTD was characterised through ITC and SPR experiments. The K_D values obtained from SPR using the Langmuir model (1.23 μM) is comparable to the value (2.28 μM), published by other groups [3]. The binding affinity of Hsp90CTD and the TPR domain of AIP (residues 166–330) has been previously characterised through ITC with reported K_D values of 13.3 μM and 18.6 μM for full length Hsp90 and an Hsp90 peptide (amino acid sequence EDASRMEEVD) respectively [8]. The lower K_D values obtained in this study (2.19 μM) using full length AIP reinforce the fact that full length proteins show binding specificity that may not always be reflected when using the individual domains or peptides [51] and in this case may reflect the dynamics of the domains in AIP or other binding possibilities we cannot yet determine (AIP N-domain with Hsp90 for example). We also demonstrate that the presence of the N-domain has a significant effect on the protein's binding affinity to its client partner, Hsp90CTD. Binding affinities of the N-domain mutants showed that the V49 M mutation decreased the protein's binding affinity by 4–5 fold. This was followed by the R16H that displayed a binding affinity around 3–4 fold lower than wild type. To our knowledge, this is the first study to investigate in-vitro the binding kinetics of full-length AIP mutants with Hsp90CTD. From a physiological viewpoint, the lowering in binding affinity, particularly observed in R16H and V49 M mutants suggests that these mutations may destabilize any complexes that require the interaction of AIP and Hsp90. Within the AIP interactome (Fig. 10), Hsp90 is present as part of AIP-Hsp90-AhR-p23 complex where it assists complex stability and maintains the AhR in a structural conformation that is receptive to ligand binding [52–54]. Destabilisation of such a complex might therefore correlate to a lowering in AhR stability and a consequent reduction in its biological function. Considering the involvement of AhR in cancer pathology, including its potential role as a tumour suppressor in the pituitary gland [55], any mutation that might directly or indirectly destabilize it, will have a detrimental effect on the cell. Similarly, Hsp90 also mediates the binding of AIP to the glucocorticoid receptor (GR), to form a multiprotein heterocomplex that also contains the co-chaperone p23, protein phosphatase 5 (PP5) and immunophilin FKBP52 [56]. Recent studies have shown that Hsp90 stabilizes GR in an active state [57] and a lowering of the AIP-Hsp90 binding affinity might destabilize the complex and therefore

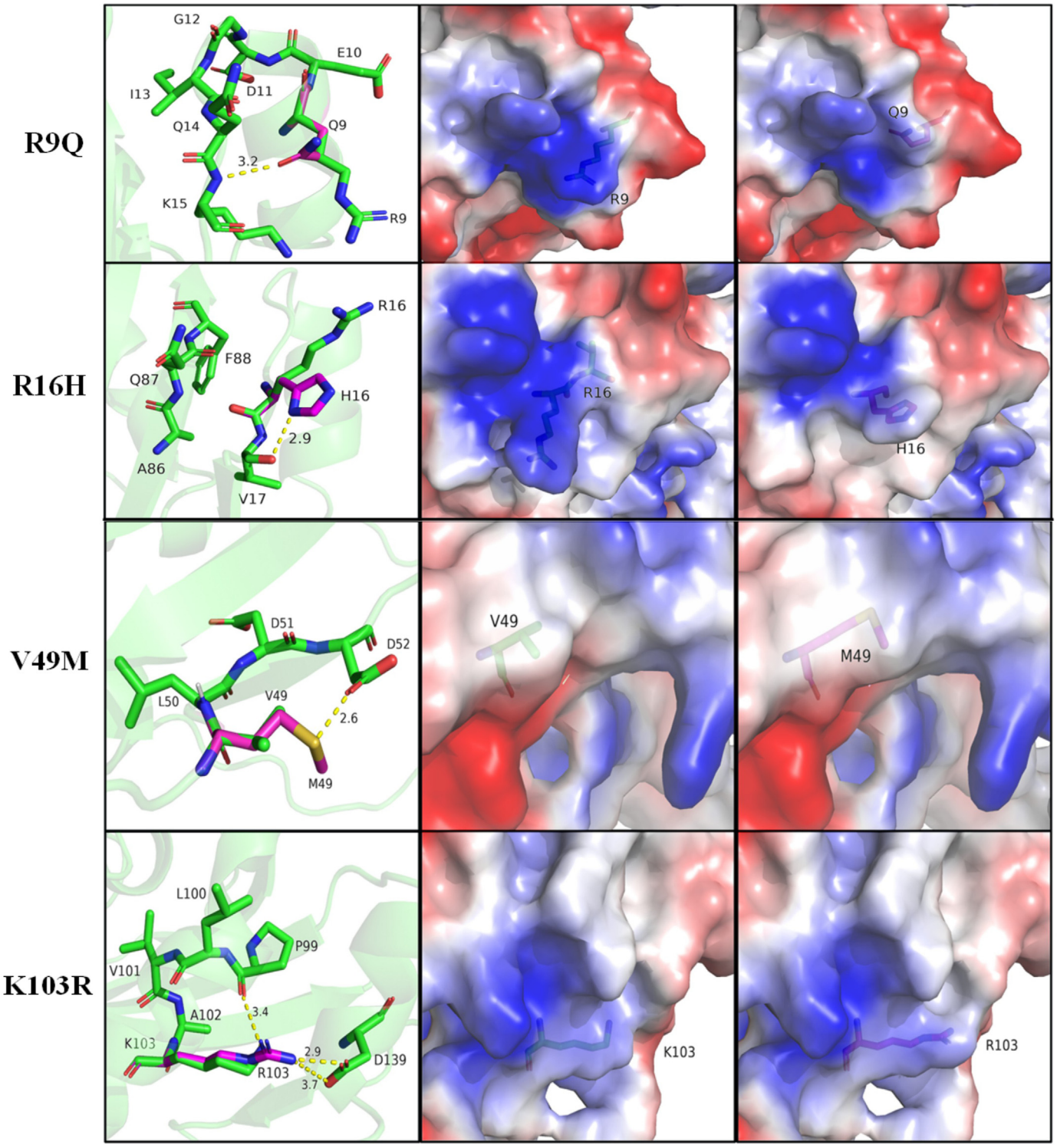

Fig. 9. Structural analyses at the site of mutation. Figures from left to right represent the amino acid interactions and the electrostatic potential around the amino acid of interest for wild type AIP protein and the mutant counterpart respectively. The carbon chain in the wild type protein is depicted in green and the side chain of the mutated reside is overlaid and carbon atoms are coloured in purple. For both wild type and mutated amino acid residue, N, O and S atoms are shown in blue, red and yellow respectively. These analyses were performed using the NMR N-domain structure (PDB 2LKN). The figure was generated using PyMol 2.6.0 and the APBS plugin [62].

affect GR-mediated transcription and signaling.

The PDE4A5 (rat) and its human homologue PDE4A4, have been shown to have a unique interaction with the co-chaperone AIP. This interaction inhibits the enzymatic activity of PDE4A5, resulting in an increase in cellular cAMP and activation of protein kinase A (PKA) [11,47]. This study is the first to kinetically characterise the interaction between AIP and PDE4A5 using full length purified proteins that show a K_D value of 2.64 μM (Table 1). This is in contrast to a previously published study whereby the interaction between the TPR domain of AIP (residues 166–330) and a short

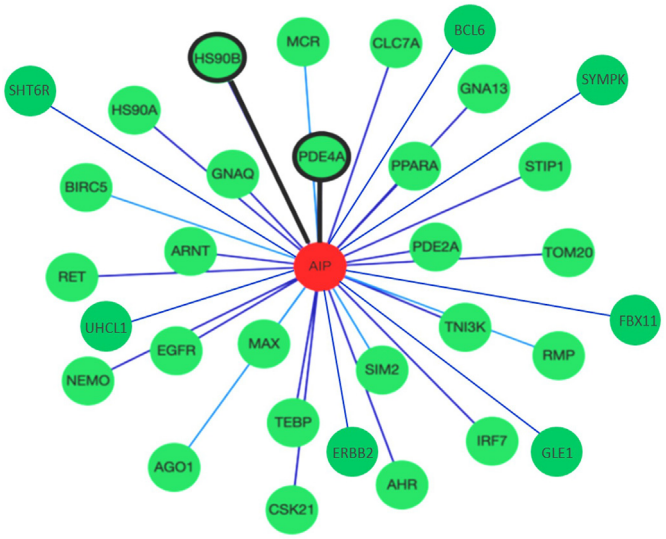

Fig. 10. AIP protein interactome c.2022. The interactions that were investigated in this study are indicated with solid black lines. This interactome was generated using the human protein-protein interaction database, PICKLE version 3.3 [64].

peptide of PDE4A5 (amino acid sequence: TLEELDW) was studied through ITC and reported a K_D value of 64.5 μM [8]. This discrepancy in value may be due to the use of short peptide sequences to examine protein:protein interactions. All mutants exhibited a lower binding affinity than the wild type. K103R and R16H showed 4–5 fold and 3-fold lowering in binding affinity respectively. This is comparable with published data investigating this interaction in yeast cells using a β-galactosidase reporter assay where a >5-fold and 2-fold difference in binding for K103R and R16H respectively was reported [12]. This current study supports this data and provides K_D values that describe the specific interaction between AIP and PDE4A5 as the sole proteins present in the mixture. Similar to the AIP-Hsp90CTD interaction, the V49 M mutant showed the least binding affinity, with a 5–6 fold difference from wild-type. This notable difference was not observed in a β-galactosidase reporter assay [12]. The reduction in binding affinity observed through SPR for AIP mutants correlates with their reduced ability to inhibit PDE4A, as measured through a PDE enzymatic assay. PDE4A was most active when incubated in the presence of V49 M and K103R, both of which also showed the lowest binding affinity through SPR. Similarly, AIP showed the strongest binding affinity and exerted the highest inhibition of enzyme activity, achieving a maximal inhibitory value of 64 %. This is comparable to the inhibition value of 62 % which has been previously reported for AIP mixed with COS7 cells over-expressing PDE4A5 [11].

Physiologically, our results would thus suggest a lowering in cellular cAMP levels in the presence of the investigated N-domain AIP mutations. Although, there is evidence that the cAMP signaling pathway is dependent on the interaction of AIP with $G\alpha_i$ proteins and does not necessarily require PDE [17,58], this does not lessen the importance and relevance of the AIP-PDE4A5 interaction. While it may not necessarily play a direct role in tumourigenesis, mutations such as the ones investigated that directly affect PDE activity and therefore its ability to regulate the cellular levels of cAMP, can affect other disease-associated pathways. Interestingly, in sporadic somatotroph adenomas with AIP mutations, the expression levels of PDE4A4 are lower than the levels present in the same adenoma sub-types with functional AIP. PDE4A4 is the human homologue of rat PDE4A5 and shares 85 % sequence homology. This decreased protein expression suggests that the presence of AIP mutations hinders the up-regulation of PDE4A4 and consequently alters the balance of the cAMP-PDE pathway [47,59,60]. This further reinforces the rationale that any change that may alter the homeostatic levels of cAMP in the cell cannot be disregarded.

The N- and C-domains of AIP had been previously characterised separately through NMR and X-ray crystallography respectively [6,8], while binding of co-chaperones containing TPR-domains has been localized to the C-terminal domain of Hsp90, the mouse AIP-like protein (AIPL1), which is 72 % homologous with AIP, has been shown to bind to Hsp90 through an unusual interaction of its N-domain [61]. Pull-down assays and NMR data have also indicated a weak interaction of the N-domain of AIP with Hsp90 [7].

Recently, a cryo-EM structure of the Hsp90-AIP-AHR cytosolic complex has been published, which reveals a closed conformation of Hsp90 dimer with AHR and AIP serving as a brace. Due to the lack of structural data, the authors report that the hinge region interconnecting the two domains of AIP was manually reconstructed [62]. In this multi protein complex, the N domain of AIP is in contact with the ligand-dependant transcription factor AhR. It was also shown that the interaction of the AIP TPR domain with the Hsp90C terminus was not as expected from peptide binding experiments as previously reported [8]. This structure is a good indication of the flexibility between AIP N and C domains which enables interaction with binding partners, as it is in contrast with our structure of AIP in solution.

Our study is the first to present the full-length AIP protein structure in solution obtained through SAXS which shows the orientation of the N- and C-domains relative to each other, and clearly demonstrates that the N domain is important for protein:-protein interactions. Analyses of the intermolecular interactions at the site of mutation showed that in all cases, the mutated residue resulted in a change in electrostatic interactions (Fig. 9). While the V49 residue is buried within the protein structure, this mutant exhibited the least binding with both binding partners. Mutagenesis experiments published by other groups showed that when adjacent core residues are replaced with methionine, the stability of the single mutants is lowered due to additional side chain flexibility [63]. Although we did not observe any changes in thermal stability, the low SPR signals observed for V49 M, as well as the low 'n' stoichiometry factor seen in ITC might suggest protein instability. This might also account for the differential behaviour shown by this mutant as also described in other studies [12,32]. Interesting, the K103R mutation resulted in the loss of a hydrogen bond and the formation of a unique bond with an amino acid residue on the αIV helix. None of the residues on the αIII helix interact with those on the αIV helix. As the flexible loop region is found between these two structural elements it can be argued that the formation of such an interaction in the K103R mutant might hinder the mobility of this loop, with possible consequence on protein-protein interactions.

5. Conclusions

Our results demonstrate the effect of N-domain mutations in the lowering of binding affinities to each of two binding proteins, Hsp90CTD and PDE4A5, also purified in this work. These effects are further supported by the differential inhibition of PDE enzyme activity by the mutants.Through this study we highlight the importance of N-domain AIP mutations in its role as a molecular co-chaperone. Given the large repertoire of binding partners for AIP it is likely that the demonstrable effect of mutations as observed in this study, will also affect other pathways that require functional AIP and thus may have an implication not only in pituitary tumorigenesis but also on other non-endocrine tumours and/or the immune system.

Funding and other information

The research disclosed in this article is partially funded by the Endeavour Scholarship Scheme, Malta (grant number 256/2015/226). Research visits to the Astbury Centre for Structural Molecular Biology, University of Leeds were financially supported by COST action CM1306 "Understanding Movement and Mechanism in Molecular Machines" and the Internationalisation Partnership Awards (IPAS+) Scheme funded by MCST awarded to Thérèse Hunter. The Mass Spectrometry Facility instrumentation used in this work is supported by BBSRC – BB/M012573/1 and the analysis was carried out by Dr James Ault. We thank the Welcome Trust (094232) and University of Leeds for the use of the Chirascan CD spectrometer (Applied Photophysics).

CRediT authorship contribution statement

Marita Vella: Writing – review & editing, Writing – original draft, Methodology, Investigation, Formal analysis, Conceptualization. **Iain W. Manfield:** Investigation, Methodology. **Brandon C. Seychell:** Investigation. **Chi H. Trinh:** Writing – review & editing, Methodology, Investigation. **Robert Rambo:** Software, Methodology, Investigation, Data curation, Writing – original draft. **G. Nasir Khan:** Investigation. **Josanne Vassallo:** Resources. **Thérèse Hunter:** Writing – review & editing, Supervision, Investigation, Conceptualization. **Gary J. Hunter:** Writing – review & editing, Writing – original draft, Supervision, Project administration, Methodology, Investigation, Funding acquisition, Formal analysis, Conceptualization.

Declaration of competing interest

The authors declare that they have no known competing financial interests or personal relationships that could have appeared to influence the work reported in this paper.

Acknowledgments

We thank Dr Robert Formosa for providing the AIP cDNA and Professor Thomas Ratajczak for the Hsp90CTD expression construct. We thank Alexander Camilleri for general technical assistance. We thank MOSBRI–Molecular Scale Biophysics Research Infrastructure (https://www.mosbri.eu/) for help and use of Mass Photometry.

Appendix A. Supplementary data

Supplementary data to this article can be found online at https://doi.org/10.1016/j.biochi.2024.09.005.

References

[1] Q. Ma, J.P. Whitlock, A novel cytoplasmic protein that interacts with the Ah receptor, contains tetratricopeptide repeat motifs, and augments the transcriptional response to 2,3,7,8-tetrachlorodibenzo-p-dioxin, J Biological Chem 272 (1997) 8878–8884, https://doi.org/10.1074/jbc.272.14.8878.

[2] L.A. Carver, C.A. Bradfield, Ligand-dependent interaction of the aryl hydrocarbon receptor with a novel immunophilin homolog in vivo, J. Biol. Chem. 272 (1997) 11452–11456, https://doi.org/10.1074/jbc.272.17.11452.

[3] J. Li, G. Zoldak, T. Kriehuber, J. Soroka, F.X. Schmid, K. Richter, J. Buchner, Unique proline-rich domain regulates the chaperone function of AIPL1, Biochemistry-Us 52 (2013) 2089–2096, https://doi.org/10.1021/bi301648q.

[4] O. Vierimaa, M. Georgitsi, R. Lehtonen, P. Vahteristo, A. Kokko, A. Raitila, K. Tuppurainen, T.M.L. Ebeling, P.I. Salmela, R. Paschke, S. Gündogdu, E.D. Menis, M.J. Mäkinen, V. Launonen, A. Karhu, L.A. Aaltonen, Pituitary adenoma predisposition caused by germline mutations in the AIP gene, Science 312 (2006) 1228–1230, https://doi.org/10.1126/science.1126100.

[5] C.A. Leontiou, M. Gueorguiev, J. van der Spuy, R. Quinton, F. Lolli, S. Hassan, H.S. Chahal, S.C. Igreja, S. Jordan, J. Rowe, M. Stolbrink, H.C. Christian, J. Wray, D. Bishop-Bailey, D.M. Berney, J.A.H. Wass, V. Popovic, A. Ribeiro-Oliveira, M.R. Gadelha, J.P. Monson, S.A. Akker, J.R.E. Davis, R.N. Clayton, K. Yoshimoto, T. Iwata, A. Matsuno, K. Eguchi, M. Musat, D. Flanagan, G. Peters, G.B. Bolger, J.P. Chapple, L.A. Frohman, A.B. Grossman, M. Korbonits, The role of the aryl hydrocarbon receptor-interacting protein gene in familial and sporadic pituitary adenomas, J Clin Endocrinol Metabolism 93 (2008) 2390–2401, https://doi.org/10.1210/jc.2007-2611.

[6] M. Linnert, K. Haupt, Y.-J. Lin, S. Kissing, A.-K. Paschke, G. Fischer, M. Weiwad, C. Lücke, NMR assignments of the FKBP-type PPIase domain of the human aryl-hydrocarbon receptor-interacting protein (AIP), Biomol Nmr Assigm 6 (2012) 209–212, https://doi.org/10.1007/s12104-012-9359-0.

[7] M. Linnert, Y.-J. Lin, A. Manns, K. Haupt, A.-K. Paschke, G. Fischer, M. Weiwad, C. Lücke, The FKBP-type domain of the human aryl hydrocarbon receptor-interacting protein reveals an unusual Hsp90 interaction, Biochemistry 52 (2013) 2097–2107, https://doi.org/10.1021/bi301649m.

[8] R.M.L. Morgan, L.C. Hernández-Ramírez, G. Trivellin, L. Zhou, S.M. Roe, M. Korbonits, C. Prodromou, Structure of the TPR domain of AIP: lack of client protein interaction with the C-terminal α-7 helix of the TPR domain of AIP is sufficient for pituitary adenoma predisposition, PLoS One 7 (2012) e53339, https://doi.org/10.1371/journal.pone.0053339.

[9] J.R. Petrulis, G.H. Perdew, The role of chaperone proteins in the aryl hydrocarbon receptor core complex, Chem. Biol. Interact. 141 (2002) 25–40, https://doi.org/10.1016/s0009-2797(02)00064-9.

[10] V. Rothhammer, D.M. Borucki, J.E. Kenison, P. Hewson, Z. Wang, R. Bakshi, D.H. Sherr, F.J. Quintana, Detection of aryl hydrocarbon receptor agonists in human samples, Sci Rep-Uk 8 (2018) 4970, https://doi.org/10.1038/s41598-018-23323-4.

[11] G.B. Bolger, A.H. Peden, M.R. Steele, C. MacKenzie, D.G. McEwan, D.A. Wallace, E. Huston, G.S. Baillie, M.D. Houslay, Attenuation of the activity of the cAMP-specific phosphodiesterase PDE4A5 by interaction with the immunophilin XAP2, J. Biol. Chem. 278 (2003) 33351–33363, https://doi.org/10.1074/jbc.m303269200.

[12] S. Igreja, H.S. Chahal, P. King, G.B. Bolger, U. Srirangalingam, L. Guasti, J.P. Chapple, G. Trivellin, M. Gueorguiev, K. Guegan, K. Stals, B. Khoo, A.V. Kumar, S. Ellard, A.B. Grossman, M. Korbonits, Characterization of aryl hydrocarbon receptor interacting protein (AIP) mutations in familial isolated pituitary adenoma families, Hum. Mutat. 31 (2010) 950–960, https://doi.org/10.1002/humu.21292.

[13] A. Nakata, D. Urano, Y. Fujii-Kuriyama, N. Mizuno, H. Itoh, K. Tago, G-protein signalling negatively regulates the stability of aryl hydrocarbon receptor, EMBO Rep. 10 (2009) 622–628, https://doi.org/10.1038/embor.2009.35.

[14] W. Cai, T.V. Kramarova, P. Berg, M. Korbonits, I. Pongratz, The immunophilin-like protein XAP2 is a negative regulator of estrogen signaling through interaction with estrogen receptor α, PLoS One 6 (2011) e25201 https://doi.org/10.1371/journal.pone.0025201.

[15] M. Vargiolu, D. Fusco, I. Kurelac, D. Dirnberger, R. Baumeister, I. Morra, A. Melcarne, R. Rimondini, G. Romeo, E. Bonora, The tyrosine kinase receptor RET interacts in vivo with aryl hydrocarbon receptor-interacting protein to alter survivin availability, J Clin Endocrinol Metabolism 94 (2009) 2571–2578, https://doi.org/10.1210/jc.2008-1980.

[16] B.H. Kang, D.C. Altieri, Regulation of survivin stability by the aryl hydrocarbon receptor-interacting protein, J. Biol. Chem. 281 (2006) 24721–24727, https://doi.org/10.1074/jbc.m603175200.

[17] I. Tuominen, E. Heliövaara, A. Raitila, M.-R. Rautiainen, M. Mehine, R. Katainen, I. Donner, V. Aittomäki, H.J. Lehtonen, M. Ahlsten, L. Kivipelto, C. Schalin-Jäntti, J. Arola, S. Hautaniemi, A. Karhu, AIP inactivation leads to pituitary tumorigenesis through defective Gαi-cAMP signaling, oncology 34 (2014) 1174–1184, https://doi.org/10.1038/onc.2014.50.

[18] A.F. Daly, M.A. Tichomirowa, P. Petrossians, E. Heliövaara, M.-L. Jaffrain-Rea, A. Barlier, L.A. Naves, T. Ebeling, A. Karhu, A. Raappana, L. Cazabat, E.D. Menis, C.F. Montañana, G. Raverot, R.J. Weil, T. Sane, D. Maiter, S. Neggers, M. Yaneva, A. Tabarin, E. Verrua, E. Eloranta, A. Murat, O. Vierimaa, P.I. Salmela, P. Emy, R.A. Toledo, M.I. Sabaté, C. Villa, M. Popelier, R. Salvatori, J. Jennings, Á.F. Longás, J.I.L. Aizpún, M. Georgitsi, R. Paschke, C. Ronchi, M. Valimaki, C. Saloranta, W.D. Herder, R. Cozzi, M. Guitelman, F. Magri, M.S. Lagonigro, G. Halaby, V. Corman, M.-T. Hagelstein, J.-F. Vanbellinghen, G.B. Barra, A.-P. Gimenez-Roqueplo, F.J. Cameron, F. Borson-Chazot, I. Holdaway, S.P.A. Toledo, G.K. Stalla, A. Spada, S. Zacharieva, J. Bertherat, T. Brue, V. Bours, P. Chanson, L.A. Aaltonen, A. Beckers, Clinical characteristics and therapeutic responses in patients with germ-line AIP mutations and pituitary adenomas: an international collaborative study, J Clin Endocrinol Metabolism 95 (2010) E373–E383, https://doi.org/10.1210/jc.2009-2556.

[19] J. Oriola, T. Lucas, I. Halperin, M. Mora, M.J. Perales, C. Alvarez-Escolá, de M.-N. Paz, G.D. Soto, I. Salinas, M.T. Julián, I. Olaizola, I. Bernabeu, M. Marazuela, M. Puig-Domingo, Germline mutations of AIP gene in somatotropinomas resistant to somatostatin analogues, Eur. J. Endocrinol./European Federation of Endocrine Societies 168 (2013) 9–13, https://doi.org/10.1530/eje-12-0457.

[20] R. Salvatori, A.F. Daly, A. Quinones-Hinojosa, A. Thiry, A. Beckers, A clinically novel AIP mutation in a patient with a very large, apparently sporadic somatotrope adenoma, Endocrinol Diabetes Amp Metabolism Case Reports 2014 (2014) 140048, https://doi.org/10.1530/edm-14-0048.

[21] E.C. Coopmans, A. Muhammad, A.F. Daly, W.W. de Herder, F.J. van Kemenade, A. Beckers, M. de Haan, A.J. van der Lely, E. Korpershoek, S.J.C.M.M. Neggers, The role of AIP variants in pituitary adenomas and concomitant thyroid carcinomas in The Netherlands: a nationwide pathology registry (PALGA) study, Endocrine 68 (2020) 640–649, https://doi.org/10.1007/s12020-020-02303-7.
[22] G. Solís-Fernández, A. Montero-Calle, M. Sánchez-Martínez, A. Peláez-García, M.J. Fernández-Aceñero, P. Pallarés, M. Alonso-Navarro, M. Mendiola, J. Hendrix, D. Hardisson, R.A. Bartolomé, J. Hofkens, S. Rocha, R. Barderas, Aryl-hydrocarbon receptor-interacting protein regulates tumorigenic and metastatic properties of colorectal cancer cells driving liver metastasis, Brit J Cancer 126 (2022) 1604–1615, https://doi.org/10.1038/s41416-022-01762-1.
[23] C.D. del Arco, L.E. Muñoz, R.B. Manchado, A.P. García, L.O. Medina, E.M. Roldán, G.S. Fernández, S.G.G. de las Heras, M.J.F. Aceñero, Prognostic role of aryl hydrocarbon receptor interacting protein (AIP) immunohistochemical expression in patients with resected gastric carcinomas, Pathol. Oncol. Res. 26 (2020) 2641–2650, https://doi.org/10.1007/s12253-020-00863-7.
[24] M.J. Fernández-Aceñero, R. Barderas, A.P. García, J. Martínez-Useros, L. Díez-Valladares, Pérez-Aguirre, L.O. Medina, S. de la S. Esteban, S. García-Botella, C.D. del Arco, C. Galindo, Aryl hydrocarbon receptor interacting protein (AIP) significantly influences prognosis of pancreatic carcinoma, Ann. Diagn. Pathol. 53 (2021) 151742, https://doi.org/10.1016/j.anndiagpath.2021.151742.
[25] S.A. Kazzaz, J. Tawil, E.W. Harhaj, The aryl hydrocarbon receptor-interacting protein in cancer and immunity: beyond a chaperone protein for the dioxin receptor, J. Biol. Chem. 300 (2024) 107157, https://doi.org/10.1016/j.jbc.2024.107157.
[26] O. Haworth, M. Korbonits, AIP: a double agent? The tissue-specific role of AIP as a tumour suppressor or as an oncogene, Br. J. Cancer 127 (2022) 1175–1176, https://doi.org/10.1038/s41416-022-01964-7.
[27] Q. Zhou, A. Lavorgna, M. Bowman, J. Hiscott, E.W. Harhaj, Aryl hydrocarbon receptor interacting protein targets IRF7 to suppress antiviral signaling and the induction of type I interferon, J. Biol. Chem. 290 (2015) 14729–14739, https://doi.org/10.1074/jbc.m114.633065.
[28] G. Schimmack, A.C. Eitelhuber, M. Vincendeau, K. Demski, H. Shinohara, T. Kurosaki, D. Krappmann, AIP augments CARMA1-BCL10-MALT1 complex formation to facilitate NF-κB signaling upon T cell activation, Cell Commun. Signal. 12 (2014) 49, https://doi.org/10.1186/s12964-014-0049-7.
[29] Z. Ozfirat, M. Korbonits, AIP gene and familial isolated pituitary adenomas, Mol. Cell. Endocrinol. 326 (2010) 71–79, https://doi.org/10.1016/j.mce.2010.05.001.
[30] G. Trivellin, M. Korbonits, AIP and its interacting partners, J. Endocrinol. 210 (2011) 137–155, https://doi.org/10.1530/joe-11-0054.
[31] A.R. Garcia-Rendueles, M. Chenlo, F. Oroz-Gonjar, A. Solomou, A. Mistry, S. Barry, C. Gaston-Massuet, M. Garcia-Lavandeira, S. Perez-Romero, M. Suarez-Fariña, A. Pradilla-Dieste, C. Dieguez, P. Mehlen, M. Korbonits, C.V. Alvarez, RET signalling provides tumorigenic mechanism and tissue specificity for AIP-related somatotrophinomas, Oncogene 40 (2021) 6354–6368, https://doi.org/10.1038/s41388-021-02009-8.
[32] R. Formosa, J. Vassallo, Aryl hydrocarbon receptor–interacting protein (AIP) N-terminus gene mutations identified in pituitary adenoma patients alter protein stability and function, Hormones and Cancer (2017) 1–11, https://doi.org/10.1007/s12672-017-0288-3.
[33] G. Hunter, T. Hunter, GroESL protects superoxide dismutase (SOD)— deficient cells against oxidative stress and is a chaperone for SOD, Health 5 (2013) 1719–1729, https://doi.org/10.4236/health.2013.510232.
[34] D. Wu, G. Piszczek, Standard protocol for mass photometry experiments, Eur. Biophys. J. 50 (2021) 403–409, https://doi.org/10.1007/s00249-021-01513-9.
[35] R. Rambo, ScÂtter Version 3.0, Supported by Diamond Light Source, Ltd, Didcot UK, 2019. http://www.bioisis.net/tutorial/9.
[36] A. Waterhouse, M. Bertoni, S. Bienert, G. Studer, G. Tauriello, R. Gumienny, F.T. Heer, T.A.P. de Beer, C. Rempfer, L. Bordoli, R. Lepore, T. Schwede, SWISS-MODEL: homology modelling of protein structures and complexes, Nucleic Acids Res. 46 (2018) gky427, https://doi.org/10.1093/nar/gky427.
[37] A.T. Brunger, Version 1.2 of the crystallography and NMR system, Nat. Protoc. 2 (2007) 2728–2733, https://doi.org/10.1038/nprot.2007.406.
[38] A.T. Brünger, P.D. Adams, G.M. Clore, W.L. DeLano, P. Gros, R.W. Grosse-Kunstleve, J.-S. Jiang, J. Kuszewski, M. Nilges, N.S. Pannu, R.J. Read, L.M. Rice, T. Simonson, G.L. Warren, Crystallography & NMR system: a new software suite for macromolecular structure determination, Acta Crystallogr Sect D Biological Crystallogr 54 (1998) 905–921, https://doi.org/10.1107/s0907444998003254.
[39] R. Khashan, W. Zheng, A. Tropsha, Scoring protein interaction decoys using exposed residues (SPIDER): a novel multibody interaction scoring function based on frequent geometric patterns of interfacial residues, Proteins Struct Funct Bioinform 80 (2012) 2207–2217, https://doi.org/10.1002/prot.24110.
[40] S.J. Fleishman, T.A. Whitehead, E.-M. Strauch, J.E. Corn, S. Qin, H.-X. Zhou, J.C. Mitchell, O.N.A. Demerdash, M. Takeda-Shitaka, G. Terashi, I.H. Moal, X. Li, P.A. Bates, M. Zacharias, H. Park, J. Ko, H. Lee, C. Seok, T. Bourquard, J. Bernauer, A. Poupon, J. Azé, S. Soner, Ş.K. Ovalı, P. Ozbek, N.B. Tal, T. Haliloglu, H. Hwang, T. Vreven, B.G. Pierce, Z. Weng, L. Pérez-Cano, C. Pons, J. Fernández-Recio, F. Jiang, F. Yang, X. Gong, L. Cao, X. Xu, B. Liu, P. Wang, C. Li, C. Wang, C.H. Robert, M. Guharoy, S. Liu, Y. Huang, L. Li, D. Guo, Y. Chen, Y. Xiao, N. London, Z. Itzhaki, O. Schueler-Furman, Y. Inbar, V. Potapov, M. Cohen, G. Schreiber, Y. Tsuchiya, E. Kanamori, D.M. Standley, H. Nakamura, K. Kinoshita, C.M. Driggers, R.G. Hall, J.L. Morgan, V.L. Hsu, J. Zhan, Y. Yang, Y. Zhou, P.L. Kastritis, A.M.J.J. Bonvin, W. Zhang, C.J. Camacho, K.P. Kilambi, A. Sircar, J.J. Gray, M. Ohue, N. Uchikoga, Y. Matsuzaki, T. Ishida, Y. Akiyama, R. Khashan, S. Bush, D. Fouches, A. Tropsha, J. Esquivel-Rodríguez, D. Kihara, P.B. Stranges, R. Jacak, B. Kuhlman, S.-Y. Huang, X. Zou, S.J. Wodak, J. Janin, D. Baker, Community-wide assessment of protein-interface modeling suggests improvements to design methodology, J. Mol. Biol. 414 (2011) 289–302, https://doi.org/10.1016/j.jmb.2011.09.031.
[41] D. Schneidman-Duhovny, M. Hammel, J.A. Tainer, A. Sali, Accurate SAXS profile computation and its assessment by contrast variation experiments, Biophys. J. 105 (2013) 962–974, https://doi.org/10.1016/j.bpj.2013.07.020.
[42] L.L.C. Schrödinger, The PyMol Molecular Graphics System 2.5, Schrödinger, LLC, 2015. https://pymol.org/2/.
[43] N. Guex, M.C. Peitsch, SWISS-MODEL and the Swiss-Pdb Viewer: an environment for comparative protein modeling, Electrophoresis 18 (1997) 2714–2723, https://doi.org/10.1002/elps.1150181505.
[44] L.H. Pearl, Review: the HSP90 molecular chaperone—an enigmatic ATPase, Biopolymers 105 (2016) 594–607, https://doi.org/10.1002/bip.22835.
[45] N. Shigapova, Z. Török, G. Balogh, P. Goloubinoff, L. Vígh, I. Horváth, Membrane fluidization triggers membrane remodeling which affects the thermotolerance in Escherichia coli, Biochem Bioph Res Co 328 (2005) 1216–1223, https://doi.org/10.1016/j.bbrc.2005.01.081.
[46] A. de Marco, L. Vigh, S. Diamant, P. Goloubinoff, Native folding of aggregation-prone recombinant proteins in Escherichia coli by osmolytes, plasmid- or benzyl alcoholoverexpressed molecular chaperones, Cell Stress Chaperon 10 (2005) 329–339, https://doi.org/10.1379/csc-139r.1.
[47] G.B. Bolger, M.F. Bizzi, S.V. Pinheiro, G. Trivellin, L. Smoot, M.-A. Accavitti, M. Korbonits, A. Ribeiro-Oliveira, cAMP-specific PDE4 phosphodiesterases and AIP in the pathogenesis of pituitary tumors, Endocr. Relat. Cancer 23 (2016) 419–431, https://doi.org/10.1530/erc-15-0205.
[48] J. Abramson, J. Adler, J. Dunger, R. Evans, T. Green, A. Pritzel, O. Ronneberger, L. Willmore, A.J. Ballard, J. Bambrick, S.W. Bodenstein, D.A. Evans, C.-C. Hung, M. O'Neill, D. Reiman, K. Tunyasuvunakool, Z. Wu, A. Žemgulytė, E. Arvaniti, C. Beattie, O. Bertolli, A. Bridgland, A. Cherepanov, M. Congreve, A.I. Cowen-Rivers, A. Cowie, M. Figurnov, F.B. Fuchs, H. Gladman, R. Jain, Y.A. Khan, C.M.R. Low, K. Perlin, A. Potapenko, P. Savy, S. Singh, A. Stecula, A. Thillaisundaram, C. Tong, S. Yakneen, E.D. Zhong, M. Zielinski, A. Žídek, V. Bapst, P. Kohli, M. Jaderberg, D. Hassabis, J.M. Jumper, Accurate structure prediction of biomolecular interactions with AlphaFold 3, Nature (2024) 1–3, https://doi.org/10.1038/s41586-024-07487-w.
[49] D. Kuo, M. Nie, A.J. Courey, Protein affinity tags, methods and protocols, Methods Mol Biology 1177 (2014) 71–80, https://doi.org/10.1007/978-1-4939-1034-2_6.
[50] L.C. Hernández-Ramírez, G. Trivellin, C.A. Stratakis, Cyclic 3′,5′-adenosine monophosphate (cAMP) signaling in the anterior pituitary gland in health and disease, Mol. Cell. Endocrinol. 463 (2018) 72–86, https://doi.org/10.1016/j.mce.2017.08.006.
[51] A. Musacchio, How SH3 domains recognize proline, Adv. Protein Chem. 61 (2002) 211–268, https://doi.org/10.1016/s0065-3233(02)61006-x.
[52] A. Kazlauskas, L. Poellinger, I. Pongratz, Two distinct regions of the immunophilin-like protein XAP2 regulate dioxin receptor function and interaction with hsp90, J. Biol. Chem. 277 (2002) 11795–11801, https://doi.org/10.1074/jbc.m200053200.
[53] N. Tsuji, K. Fukuda, Y. Nagata, H. Okada, A. Haga, S. Hatakeyama, S. Yoshida, T. Okamoto, M. Hosaka, K. Sekine, K. Ohtaka, S. Yamamoto, M. Otaka, E. Grave, H. Itoh, The activation mechanism of the aryl hydrocarbon receptor (AhR) by molecular chaperone HSP90, FEBS OPEN BIO 4 (2014) 796–803, https://doi.org/10.1016/j.fob.2014.09.003.
[54] I. Kudo, M. Hosaka, A. Haga, N. Tsuji, Y. Nagata, H. Okada, K. Fukuda, Y. Kakizaki, T. Okamoto, E. Grave, H. Itoh, The regulation mechanisms of AhR by molecular chaperone complex, J. Biochem. 163 (2017) 223–232, https://doi.org/10.1093/jb/mvx074.
[55] R. Formosa, J. Borg, J. Vassallo, Aryl hydrocarbon receptor (AHR) is a potential tumour suppressor in pituitary adenomas, Endocr. Relat. Cancer 24 (2017) 445–457, https://doi.org/10.1530/erc-17-0112.
[56] I. Grad, D. Picard, The glucocorticoid responses are shaped by molecular chaperones, Mol. Cell. Endocrinol. 275 (2007) 2–12, https://doi.org/10.1016/j.mce.2007.05.018.
[57] C.M. Noddings, R.Y.-R. Wang, J.L. Johnson, D.A. Agard, Structure of Hsp90–p23–GR reveals the Hsp90 client-remodelling mechanism, Nature 601 (2022) 465–469, https://doi.org/10.1038/s41586-021-04236-1.
[58] R. Formosa, A. Xuereb-Anastasi, J. Vassallo, Aip regulates cAMP signalling and GH secretion in GH3 cells, Endocr. Relat. Cancer 20 (2013) 495–505, https://doi.org/10.1530/erc-13-0043.
[59] M.F. Bizzi, S.V.B. Pinheiro, G.B. Bolger, J.R. de O.L. Schweizer, A.V. Giannetti, M.N. Dang, A. Ribeiro-Oliveira, M. Korbonits, Reduced protein expression of the phosphodiesterases PDE4A4 and PDE4A8 in AIP mutation positive somatotroph adenomas, Mol. Cell. Endocrinol. 476 (2018) 103–109, https://doi.org/10.1016/j.mce.2018.04.014.
[60] M.F. Bizzi, G.B. Bolger, M. Korbonits, R.-O. A Jr., Phosphodiesterases and cAMP pathway in pituitary diseases, Front. Endocrinol. 10 (2019) 141, https://doi.org/10.3389/fendo.2019.00141.
[61] D. Srivastava, R.P. Yadav, S. Singh, K. Boyd, N.O. Artemyev, Unique interface and dynamics of the complex of HSP90 with a specialized cochaperone AIPL1, Structure 31 (2023) 309–317.e5, https://doi.org/10.1016/j.str.2022.12.014.
[62] J. Gruszczyk, L. Grandvuillemin, J. Lai-Kee-Him, M. Paloni, C.G. Savva, P. Germain, M. Grimaldi, A. Boulahtouf, H.-S. Kwong, J. Bous, A. Ancelin,

C. Bechara, A. Barducci, P. Balaguer, W. Bourguet, Cryo-EM structure of the agonist-bound Hsp90-XAP2-AHR cytosolic complex, Nat. Commun. 13 (2022) 7010, https://doi.org/10.1038/s41467-022-34773-w.

[63] M. Senda, S. Muto, M. Horikoshi, T. Senda, Effect of leucine-to-methionine substitutions on the diffraction quality of histone chaperone SET/TAF-Iβ/INHAT crystals, Acta Crystallogr. Sect. F 64 (2008) 960–965, https://doi.org/10.1107/s1744309108028704.

[64] A. Gioutlakis, M.I. Klapa, N.K. Moschonas, Pickle 2.0: a human protein-protein interaction meta-database employing data integration via genetic information ontology, PLoS One 12 (2017) e0186039, https://doi.org/10.1371/journal.pone.0186039.